Microcurvature landscapes induce neural stem cell polarity and enhance neural differentiation

Ho-Yin Yuen, Wai-Sze Yip, Suet To & Xin Zhao

Abstract

Tissue curvature has long been recognized as an important anatomical parameter that affects intracellular behaviors, and there is emerging interest in applying cell-scale curvature as a designer property to drive cell fates for tissue engineering purposes. Although neural cells are known to undergo dramatic and terminal morphological changes during development and curvature-limiting behaviors have been demonstrated in neurite outgrowth studies, there are still crucial gaps in understanding neural cell behaviors, particularly in the context of a three-dimensional (3D) curvature landscape similar to an actual tissue engineering scaffold. In this study, we fabricated two substrates of microcurvature (curvature-substrates) that present a smooth and repeating landscape with focuses of either a concave or a convex pattern. Using these curvature-substrates, we studied the properties of morphological differentiation in N2a neuroblastoma cells. In contrast to other studies where two-dimensional (2D) curvature was demonstrated to limit neurite outgrowth, we found that both the concave and convex substrates acted as continuous and uniform mechanical protrusions that significantly enhanced neural polarity and differentiation with few morphological changes in the main cell body. This enhanced differentiation was manifested in various properties, including increased neurite length, increased nuclear displacement, and upregulation of various neural markers. By demonstrating how the micron-scale curvature landscape induces neuronal polarity, we provide further insights into the design of biomaterials utilizing the influence of surface curvature in neural tissue engineering.

Graphic abstract

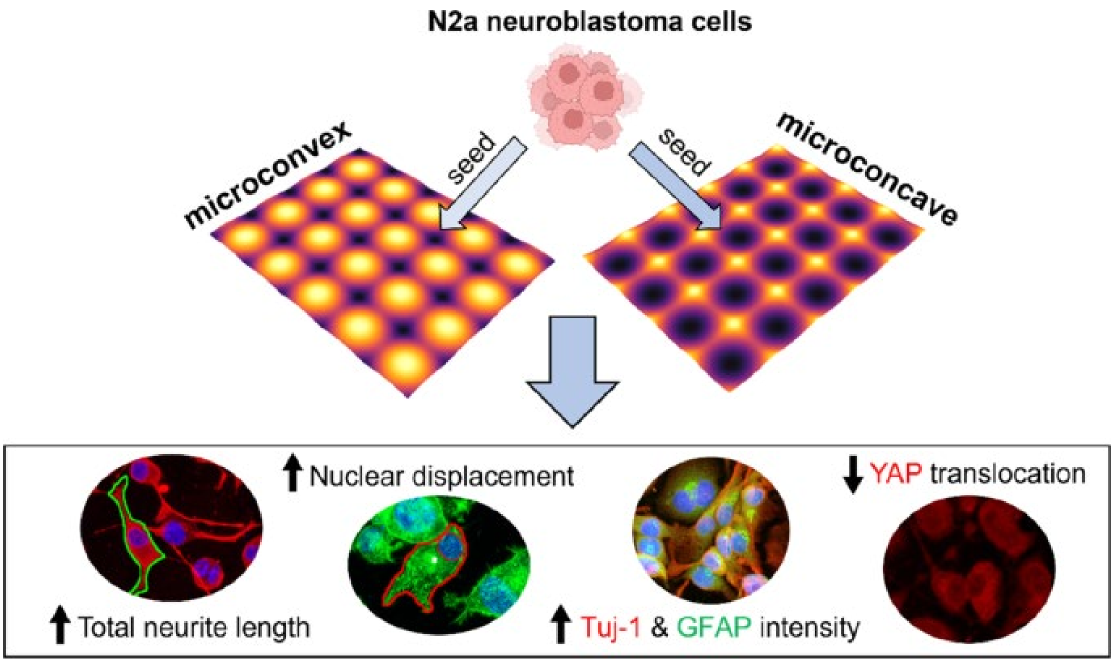

Introduction

Although tissue curvature was recognized as an important anatomical parameter that influences intracellular behaviors several decades ago [1, 2], its mechanism relies on a wide range of substrate factors beyond just the degree of curvature, including the surface roughness, material stiffness, and surface chemical composition [3]. With many mechanical studies that have decoupled the various roles in fundamental substrate mechanics [4, 5, 6, 7], surface curvature is now modeled to be an independent factor that induces cell fates for tissue engineering purposes [8, 9]. Among possible applications, scaffolds for neural engineering have been investigated [10] due to the realization that brain tissues possess a mechanical microenvironment that exhibits a wide range of curvatures that could influence intracellular arrangement [11, 12]. Indeed, several studies have observed curvature as a limiting factor for neurite outgrowth, including curved channels of single-cell neurite outgrowth [13], microrods of varying curvature [14, 15], and circular grooves for neural cell seeding [10]. However, tissue engineering scaffolds are usually designed as biomimetic three-dimensional (3D) microenvironments that allow arbitrary tissue integration, which is how current studies were formulated to utilize curvature scaffolds for osteogenesis purposes [16, 17, 18, 19], and there is a lack of similar mechanical studies for neural cells [20]. Therefore, it remains to be elucidated how a substrate of repeating curvature patterns can influence neural differentiation.

In this study, we defined two microcurvature patterns, the microconcave pattern and the microconvex pattern, where they are mathematically opposite of one another so that we can study their effects on neural cells differentially. The patterns were fabricated onto a silicone substrate as a continuous and repeating curvature terrain, where cells were seeded onto them and continuously stimulated as they adhered, migrated, proliferated, and differentiated (Fig. 1a). We focused our experiments on neural differentiation since we are interested in how curvature influences the fate of neural stem cells, which dictates distinct functions as neurons, astrocytes, or some other neural cell types [21]. This would provide key understandings of how curvature can be taken advantage of for neural tissue engineering, where their goals were to improve efficacy in regeneration by guiding cellular identity [22, 23].

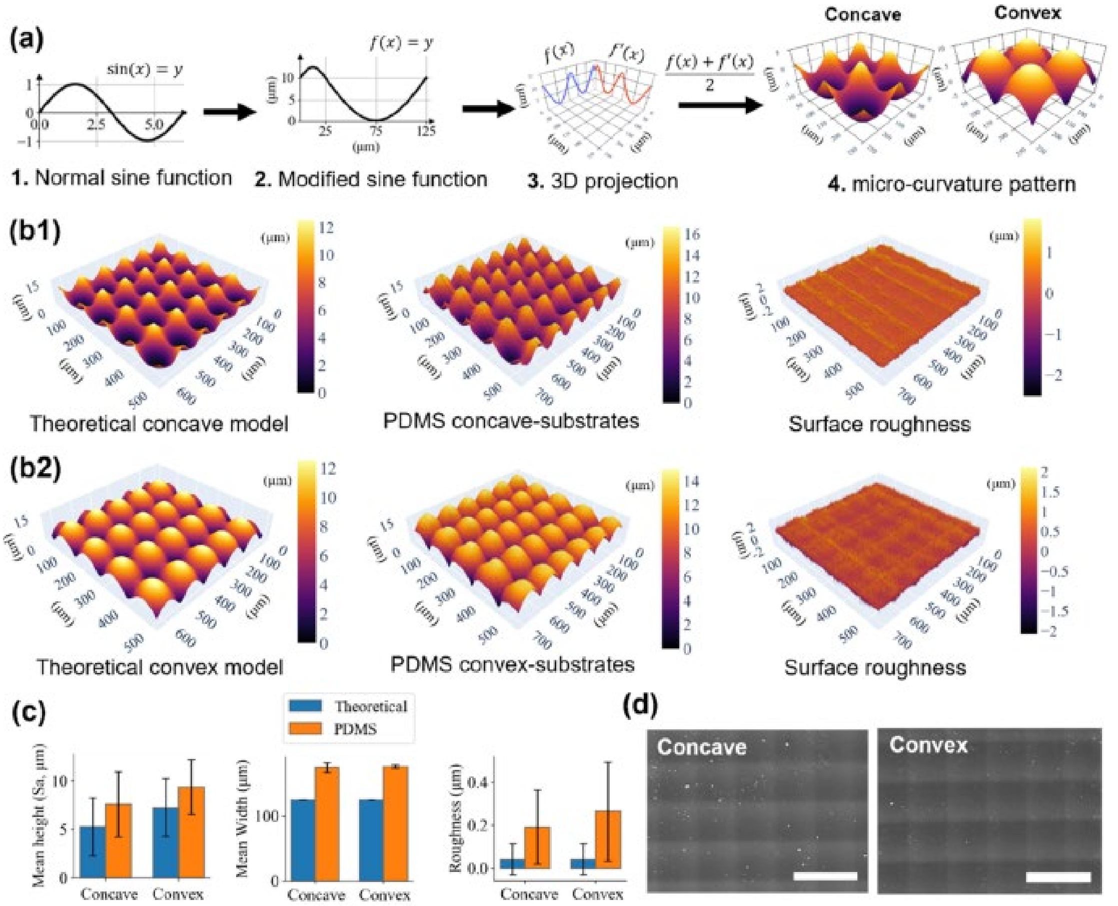

Fig. 1

Design and surface characterization of the curvature-substrates. **a** Parameters and designs of the microcurvature pattern. **b1**, **b2** Data generated from the 3D laser microscope. The 3D surface plots of the measured curvature-substrates are constructed along with the surface roughness plot derived using a Savitzky-Golay filter and the theoretical surface curvature model for comparison. **c** Key roughness parameters of the curvature-substrates against their theoretical (ideal) models. **d** Representative SEM images of the curvature-substrates. Scale bar: 200 μm. Error bars are standard deviations. PDMS: polydimethylsiloxane; SEM: scanning electron microscope

The article is organized as follows: we first introduce the designs of the microconcave and microconvex patterns. We mathematically defined these patterns as a 3D sinusoidal function and modified them to express either a continuous surface concave pattern or a continuous surface convex pattern (hereafter referred to collectively as curvature-substrates) and characterized their surface roughness profile. Next, we seeded N2a neuroblastoma cells on the curvature-substrates, induced their differentiation and observed different morphological and physical properties of the cells. We found that the cells primarily had increased neurite length and nuclear displacement on the curvature-substrates, demonstrating enhanced neural polarity. Finally, we evaluated their differentiation biomarkers (Tuj-1 and GFAP) to similarly conclude an improved effect on neural differentiation. Through this study, we provide the physical details and behaviors of neural cells under the effect of curvature, leading to curvature as potentially an integrated biophysical cue for biomaterial design in neural tissue engineering.

Materials and methods

Curvature-micropatterned mold machining

The curvature-micropatterned mold (both a concave mold and a convex mold) with dimensions of 1 cm×1 cm×1.5 cm (width×length×height) was fabricated by ultraprecision machining with fast-tool-servo assisted diamond turning technology on brass molds. The four-axis ultraprecision machine (Moore Nanotech 350FG) in the State Key Laboratory of Ultra-Precision Machining Technology of The Hong Kong Polytechnic University was used. The surface roughness and surface topology of the molds were then measured using an optical profiling system (Zygo NexView), as shown in Fig. S1 (Supplementary Information).

Curvature-micropatterned polydimethylsiloxane substrate (curvature-substrate) fabrication

The curvature-micropatterned substrate in the form of a cell culture well (curvature-substrate) was fabricated using a standard soft lithography process with silicone polydimethylsiloxane (PDMS) [24]. Briefly, the PDMS prepolymer solution (Sylgard 184, Dow Corning, MI, USA) was mixed uniformly with curing agents at a mass ratio of 10:1. Then, the brass mold was submerged into the solution, and the air bubbles trapped during this process were removed via a vacuum chamber. After curing at 80 °C for at least two hours, a curvature substrate (either a concave substrate or a convex substrate) with a size of 1 cm^2 square was generated.

Curvature-substrate surface characterization

A 3D laser scanning microscope (Keyence VK-X200, USA) was used to obtain the surface roughness profile of the curvature-substrates from a random spot at 10×magnification, and a scanning electron microscope (SEM, Tescan VEGA3, Czech Republic) was used to visualize the surface morphology of a random spot at the microscale. The raw data of the surface roughness profile were first extracted from the data file using vk4-python-driver (https://github.com/torkian/vk4-python-driver) and then processed using a custom Python script to obtain the measurements. Mean height refers to the conventional arithmetical mean height (Sa), mean width was defined as the distance between the peaks of concave pits or pits of convex hills along the x and y axes using a typical peak-finding algorithm in [25], and roughness was defined as the difference to the corresponding data point along the x axis that was fitted to a Savitzky-Golay filter with a window size of 51 and a polynomial order of three.

Cell culture

The mouse Neuro2a neuroblastoma cell line (N2a, ATCC, USA) was cultured in complete growth media composed of 89% high glucose Dulbecco's modified Eagle medium (DMEM), 10% fetal bovine serum (FBS), and 1% penicillin–streptomycin solution (pen-strep), as recommended by the supplier (iCell-m040, GuangZhou Biolink Technology Co., Ltd., Guangzhou, China). During incubation, the medium was replaced every two days, and the cells were subcultured once in confluence. For the differentiation of N2a cells, we followed a common protocol [26, 27] based on serum deprivation and retinoic acid stimulation by using a differentiation medium composed of 98% high glucose DMEM, 1% FBS, and 10 μmol/L retinoic acid.

Cell seeding on curvature-substrates

Laminin solution (rh-Laminin521, 100 μg/mL, Thermo Fisher, USA) was diluted in 1 μg/cm^2 Hanks' balanced salt solution (HBSS) to coat the curvature substrate overnight at 4 °C to promote cell adhesion. Before cell seeding, the laminin solution was removed from the curvature substrate and gently rinsed with warm phosphate buffered saline (PBS) twice. Then, N2a cells between the 5th and 10th passages were first seeded onto curvature-substrates with growth medium at 5000 cells/cm^2 for one day and then replaced with differentiation medium the next Day (marking Day 0). At least three replicates were used for each type of curvature substrate (concave, convex, or flat).

Immunocytochemistry

The procedures were performed at room temperature, and the samples were rinsed with PBS between every step at least twice with a 3-min interval. Briefly, the medium was removed from the sample and then fixed using 4% paraformaldehyde in PBS (PFA) for 20 min. The cells were then permeabilized with 0.1% Triton in PBS for 20 min. Finally, the samples were blocked with 1% bovine serum albumin (BSA) in PBS for 45 min and stored at 4 °C in PBS for a maximum of two days before further procedures.

There were two sets of samples for each experimental group for a parallel study of two different sets of immunofluorescent markers. The first set of markers was the YAP and F-actin markers (i.e., morphological markers), and the second set was the Tuj-1 and GFAP markers (i.e., neural markers). For the first set of markers, rabbit anti-YAP (1:200, Proteintech, China) and Alexa Fluor 488-conjugated phalloidin (1:500, Thermo Fisher, USA) were prepared by dilution in blocking buffer. The diluted anti-YAP was first incubated with the samples at 4 °C overnight, and then the diluted phalloidin was incubated with the samples at room temperature for 45 min. The secondary antibody, goat pAb to rabbit 635 red-conjugated (Abcam, 1:1000, UK), was then diluted into blocking buffer with the samples for 1 h at room temperature in the dark. For the second set of markers, mouse anti-Tuj-1 (GeneTex, 1:500, USA) and rabbit anti-GFAP (GeneTex, 1:500, USA) were diluted in blocking buffer and incubated with the samples at

4 °C overnight. Then, the secondary antibodies, goat pAb to mouse 594 Red-conjugated (Abcam, 1:1000, USA) and goat pAb to rabbit 488 fluorescein-isothiocyanate (FITC)-conjugated (Abcam, 1:1000, USA), were diluted into blocking buffer and incubated for 1 h at room temperature in the dark. Finally, both sets of samples were stained with 4',6-diamidino-2-phenylindole (DAPI, 1:2000, Thermo Fisher, USA) for 3 min and mounted under a microscope for quantification.

Quantitative methods for immunocytochemistry

To extract morphological and fluorescence measurements from each single cell, the following protocol was devised. For each experimental group, we contained at least three replicates, and each replicate had at least two *z*-stacked (3D) images captured using a confocal microscope (Leica TCS SPE, German); see Table S1 (Supplementary Information) for the sample size. We first labeled each single cell using a cell segmentation algorithm, Cellpose [28]. The images were max-projected into two-dimensional (2D) plane, and the nucleus for each cell was labeled using the "nuclei" model by Cellpose. For the F-actin-stained area and Tuj-1-stained area, two self-trained models were used: nine representative images (out of 78 for actin images and out of 84 for Tuj-1 images) were used to further train the pretrained "CP" model by Cellpose so that it could segment the neurites of the cells from the images better. The YAP-stained area and GFAP-stained area were labeled using the direct results of the actin segmentation and Tuj-1 segmentation, respectively. Based on the 2D segmentation, we computed the 3D segmentation by labeling the voxel of each single cell using the default autothreshold method in ImageJ.

Based on the 2D and 3D segmentation of each single cell with either its F-actin- and YAP-stained region or its Tuj-1- and GFAP-stained region at the same time, various measurements were computed in Python. For integrated fluorescence intensity (e.g., YAP intensity), we first computed a normalized measure of DAPI intensity (normalized against the 405 nm laser power and the DAPI-stained area). Then, a sum of the pixel intensity of the protein signal (e.g., YAP fluorescence) was computed and normalized against its laser power (for YAP, 635 nm) and the normalized DAPI intensity. This obtained the integrated intensity independent of the confocal laser strength and its *z*-position on the substrate. Based on our segmentation, we also characterized the neurite features of each single cell based on the concept in [29]. Briefly, we skeletonized [30] the F-actin-stained area and Tuj-1-stained area and considered a branch as a neurite if its length from its attachment point (the point where it sprouts from the nucleus) to an ending point (terminating point of a branch) exceeded the major axis length of its nucleus. Neurite complexity is defined as the ratio of the number of ending points to the number of attachment points.

Statistical analysis

All statistical significance tests were computed by the Scipy package [25] in Python. Welch's *t* test was used for statistical tests of any two samples unless otherwise stated, and the Pearson correlation coefficient was computed for any correlation test. The threshold of the *p* values for statistical significance is noted in the relevant figures. The error bars either express the standard deviation or the error at the 99% confidence interval (ci) (computed based on bootstrapping), as noted correspondingly. For all samples, data points that were higher than or equal to the 99% quantile were considered outliers and removed unless otherwise stated.

Results

Curvature-substrate designs and characterizations

To induce a microcurvature effect on cells in general, our micropatterned landscapes should fulfil two criteria: the microcurvature (for both concave and convex) should have a depth (height) and width that are at least bigger than the cells so that the cells can sense active perturbations from the substrate [3, 16], and the stimulation from the microcurvature should be sufficiently (but not overly) mild so that the cells maintain an even distribution across the curvature-substrate similar to a flat substrate [17]. In this study, we modeled the substrate surface based on a 3D sinusoidal function (similar design was also used in [17]), where we further modified the function so that we can emphasize either its concave feature or its convex feature. Figure 1a demonstrates our design. First, to emphasize the concave feature, we defined the width and height of the concave part in a sine wave twice as large as the convex part, and the same applies when we instead emphasize the convex feature. For the actual size of the micropattern, we considered the physical measurements of our cell model, Neuro-2a, where it has been reported that the cells usually have a diameter ranging from 20 to 50 μm [31]. We also referred to similar systemic curvature studies, where several studies have defined curvature $\kappa=0.01$�$=0.01$ (or -0.01), a moderate value that induced changes in cell fates (e.g., improved osteogenesis [16], neurite-limiting microrods [14] and microchannels [10]). We, therefore, defined the concave pit or the convex hill to have a width of 100 μm and a height of 10 μm, which yield a maximum curvature κ� of ≈≈0.01 (concave) or -0.01 (convex) (see Supplementary Information S1 for full definition). Using a comparable design parameter to other studies, this allowed us to establish similar hypotheses and investigate from here on how curvature affects neural cells similarly and differently.

An ultraprecision machine with a nanometric level was used (Sect. "Curvature-micropatterned mold machining") to fabricate the micropattern molds, and the resulting profiles of the microcurvature molds are shown in Fig. S1 (Supplementary Information). Briefly, both the microcurvature molds had a maximum height (Sz) of approximately 13 μm, which was within 1 μm of the theoretical height (12 μm), demonstrating their form accuracy. Using the mold, we obtained the PDMS curvature substrate via replica molding, and Figs. 1b1, 1b2, and 1d show the resulting measurements. In terms of the major features of the curvature-substrates, the 3D surface retained its fidelity compared to the theoretical curvature model, where both a continuous surface of concave pits and a continuous surface of convex hills can be observed on the concave substrate and the convex substrate, respectively. We also obtained their surface roughness plot to evaluate its surface accuracy (Figs. 1b1 and 1b2). Here, we observed that the regions with high roughness followed a distinct and universal grid-like pattern aligned with the minor features of the 3D surface plots (i.e., the minor convex hills between the major concave pits for concave substrates and similarly for convex substrates), which can be attributed to the imperfections of PDMS molding at a micrometric scale. In Fig. 1c, we can also see that the errors from the theoretical models were minimal, where the standard deviations for both the mean height and mean width of the curvature-substrates were similar to those of the theoretical models and that both the height and width have a similar difference compared to the theoretical values (roughly 30% higher), further showing a consistent but minimal demolding imperfection.

Changes in whole-cell morphology of neural cells on curvature-substrates

After the fabrication of the curvature-substrates (i.e., concave substrate, convex substrate, and flat substrate), we then seeded the cells onto them and incubated the cells with differentiation medium to observe their phenotypic changes. The N2a neuroblastoma cell line was used as the model and differentiated using a protocol of serum deprivation and retinoic acid stimulation (10 μmol/L) [27, 32], which induces growth arrest and activates morphological differentiation [33, 34]. Samples were examined after 1, 2, 3, or 5 days of differentiation (details in Sect. "Cell seeding on curvature-substrates"). Figure 2a shows a representative sample of the F-actin-stained cells in each experimental group, and one apparent feature was the higher cell density in the flat substrate compared to the concave and convex substrates among all groups (Days 1, 2, 3, and 5). This could be attributed to either the increased surface area or a reduced proliferation (due to better differentiation) of the curvature groups. We also evaluated the degree of neurite outgrowth in our samples, a key phenotype of neural differentiation. Qualitatively, we observed improved neurite outgrowth in curvature groups on Day 3 and Day 5 (Fig. 2a). Importantly, our measurements (Fig. 2b) showed that the total neurite length in the curvature groups was indeed significantly higher. This demonstrated a promising curvature effect on neural differentiation.

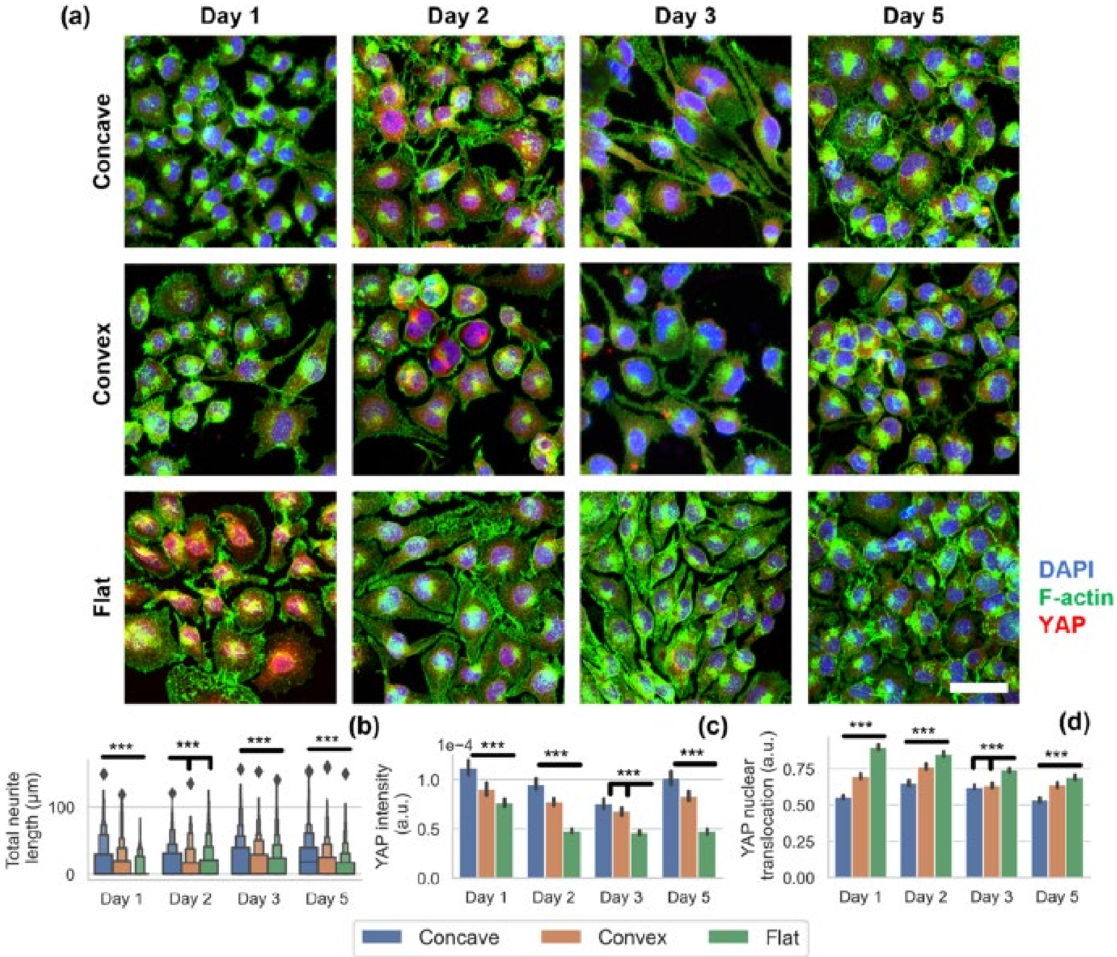

Fig. 2

Representative samples and measurements related to the mechanotransduction of cells in each group. **a** Representative$z$-projected fluorescent samples with nuclear (blue), F-actin (green), and YAP (red) staining (scale bar: 50 μm). **b** Boxen plots illustrate the population distribution of the total neurite length of each group. **c** The mean integrated intensity of the YAP-stained area among the cells in each group (see Sect. ″Quantitative methods for immunocytochemistry″ for computation details). **d** The mean ratio of the YAP intensity in the nuclear region to the YAP intensity in the cytoplasmic region among the cells in each group. This expresses the level of YAP translocated into the nucleus. A horizontal statistical bar indicates statistical significance among all pairs of samples (otherwise only the indicated pairs), ***$p<0.001$. The error bar indicates ci=99%

We then evaluated the morphological changes in the neural cells. Typically, morphological changes indicate the activation of mechanotransduction [35]; e.g., an increased cell spreading area correlates with focal adhesion that rearranges the F-actin cytoskeleton for gene expression [36, 37]. Figure S2 (Supplementary Information) shows the physical measurements we examined for mechanical changes in the cells. Although we found that the cell volume (Fig. S2b in Supplementary Information) in the curvature groups was significantly higher (likely due to the vertical variation in the substrate), we did not find consistent differences in cell area (i.e., spreading area, Fig. S2a in Supplementary Information). We also evaluated the cell shape and positioning in our samples, which could indicate nuclear deformation (another strong curvature factor that induces mechanotransduction [38]). Similarly, however, we also did not find any consistent difference in nucleus diameter and area among different groups (Figs. S2c and S2d in Supplementary Information) or in the *z*-level of cells between concave and convex groups (Fig. S2e in Supplementary Information). Considering existing curvature studies associated nuclear deformation with changes in nuclear morphology (e.g., nucleus was "stressed" when positioned on top of convex patterns [16, 17]), with no significant differences in the nucleus diameter, area, and *z*-level for cells in curvature groups, nuclear deformation (and its effect) is likely not induced in cells on the curvature-substrates. Similarly, we did not find a difference in cell eccentricity (shape) in different groups (Fig. S2f in Supplementary Information), indicating that the cell bodies may not be deformed by the curvature. The absence of a typical curvature effect may be attributed to our curvature design. Although the cell diameter was relatively small (on average twice as small) compared to the major concave or convex features (Fig. S2g in Supplementary Information), the cell heights slightly exceeded the curvature height (Fig. S2h in Supplementary Information); hence, without a larger size or degree of curvature, the micropatterns may not have exerted their mechanical effect (e.g., "stressed") on the main cell bodies.

Changes in mechanotransduction of neural cells on curvature-substrates

Despite the significant difference in neurite outgrowth, since we found that there was little morphological difference between cells on curvature-substrates and flat substrates, we further characterized more specifically the protein expression of YAP to examine events of mechanotransduction. YAP is one of the ubiquitous mechano-sensing proteins [39, 40] that is expressed in response to changes in cytoskeleton arrangements (due to mechanical factors). Additionally, YAP was shown to be downregulated during neuronal differentiation [41,42,43]. As shown in Fig. 2c, although we found a higher YAP intensity in the curvature-substrates compared to flat substrates across different groups, Fig. 2d showed that they were actually cytoplasmic expression instead of nuclear expression (i.e., not translocated into the nucleus). This actually implies inhibition of YAP expression in the curvature-substrates, showing results consistent with the literature that neuronal differentiation is activated by the inhibition of YAP, as noted above, and additionally consistent with our data where there were improved neurite outgrowth. Regarding the difference between concave and convex substrates, although some significance can be identified, it is neither consistent nor comparable to the significant difference compared to the flat substrates.

Changes in the nuclear positioning of neural cells on curvature-substrates

Since there was indeed a significant difference in mechanotransduction as evaluated above, we examined other possible subcellular changes that can be influenced mechanically to identify the effect of curvature. The nucleus is a major mechano-sensing unit since it is one of the stiffer components of a cell [44], and nuclear positioning is a process that can be induced mechanically to introduce polarity in differentiating cells [45, 46]. Such processes are essential to establish neuronal polarity for neurite outgrowth and neuronal differentiation [47, 48]. We therefore computed the nuclear displacement for our samples, as shown in Fig. 3. Indeed, the curvature groups have a significantly higher mean nuclear displacement compared to the flat groups (Fig. 3b), although similar to other data, the difference between the concave and convex substrates was not as significant. We also examined the top 10 cells with the highest nuclear displacement in each group (Fig. 3a); however, we did not find cells in different groups to have particularly distinct morphology or displacement. Overall, our data showed that there were more cells with higher nuclear displacement in the curvature groups than in the flat groups.

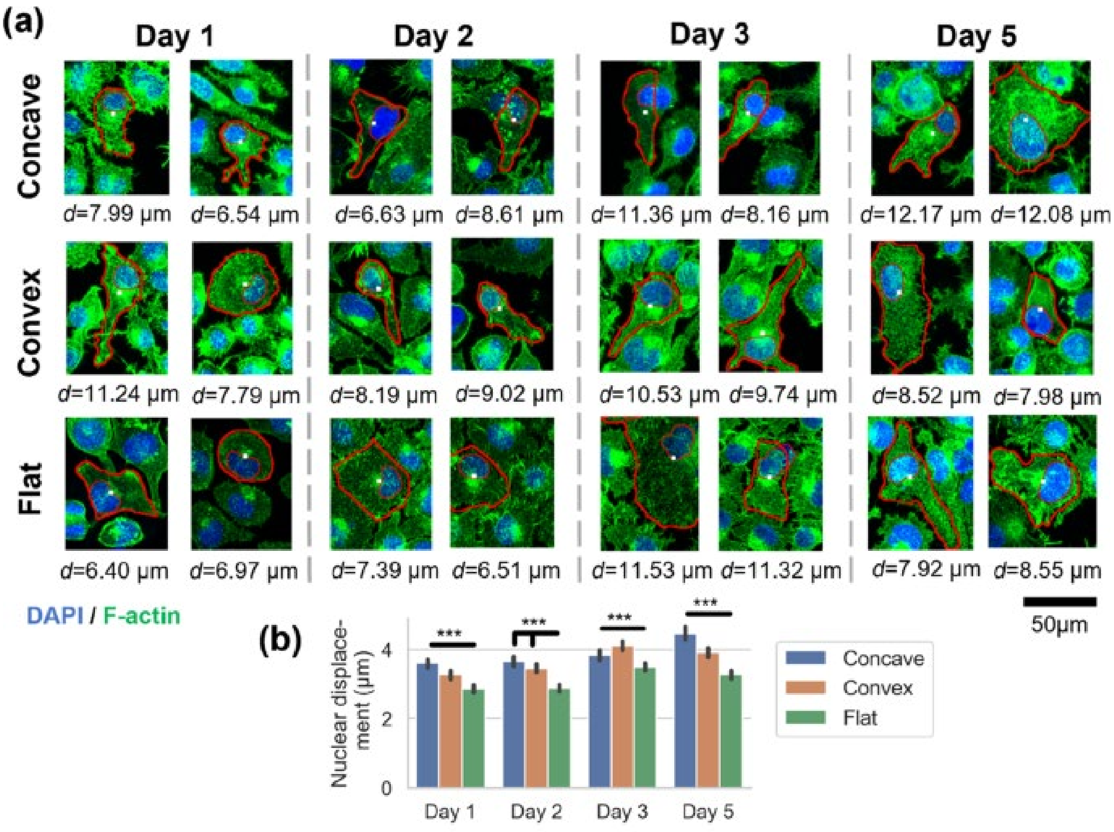

Fig. 3

Nuclear positioning of neural cells on curvature-substrates. **a** *z*-projected representative samples. In each group, 10 samples with the highest nuclear displacement were examined, and two representative samples were selected for the figures. The outer red outline depicts the F-actin-stained component, the inner red outline depicts the nuclear component, and the white dot depicts the centroid based on the YAP-stained area, determined algorithmically (*d* shows the displacement distance). **b** Mean nuclear displacement for all cells in each group. A horizontal statistical bar indicates statistical significance among all pairs of samples (otherwise only the indicated pairs), ***$p<0.001$. The error bar indicates ci=99%

Associations of mechanical changes in neural cells on curvature-substrates

Although we identified that curvature-substrates were able to influence their cells in various aspects (e.g., physical measurements, mechanotransduction, and nuclear displacement), it was unclear whether these changes manifested synergically in the same groups of cells and whether there were other mechanisms (apart from curvature as a mechanical stimulus) that influenced the outcome of the curvature groups. To this end, we first examined the distance of the nearest neighbor (DNN) for cells in different groups. DNN is often used to characterize the effect of contact inhibition between cells [49, 50, 51], and in our case, it may influence the cell behaviors if the lower surface area of the flat substrates limits the behaviors of its cells. Figure 4a shows the mean distance to the nearest neighbor of different groups. Apart from a difference on Day 1 where the curvature groups had a lower distance than the flat groups, the rest of the groups had insignificant differences, indicating that the effect from the increased surface area in the curvature-substrates was minimal (the slight difference on Day 1 could be attributed to a mild cell colony-arranging effect by the curvature pattern initially).

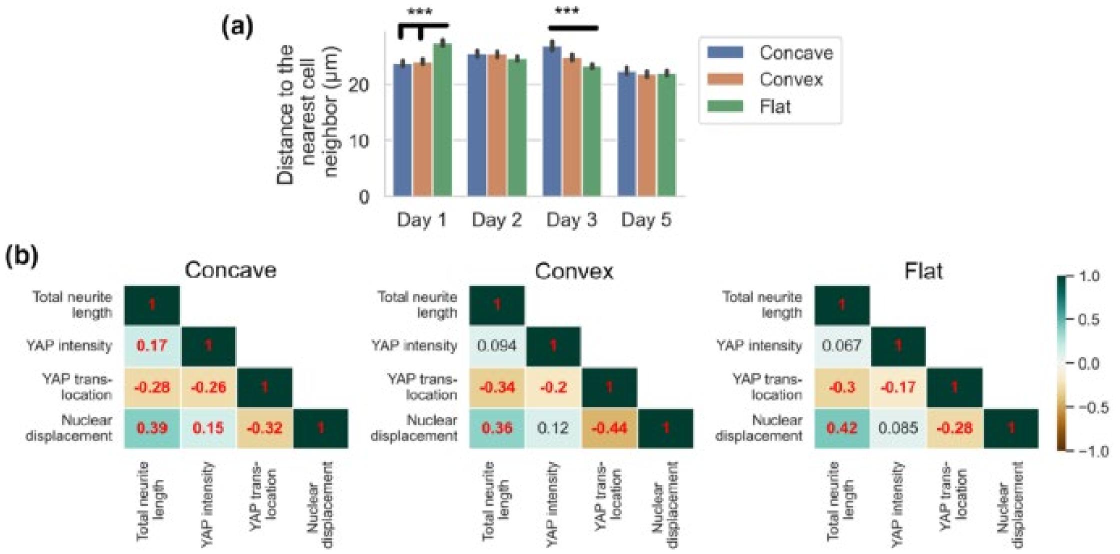

Fig. 4

a Mean distance to the nearest cell neighbor for each group. For each cell, the cell with the minimum Euclidean distance to itself was obtained, and the distance was calculated using the nucleus centroid. A horizontal statistical bar indicates statistical significance among all pairs of samples (otherwise only the indicated pairs), ***$p<0.001$. The error bar indicates ci=99%. **b** Heatmap illustrating the linear correlation between the measurements of the corresponding group. The number denotes the Pearson r coefficient (denoted also by the color of the tile) and is highlighted in red if it is statistically significant ($p<0.001$). We consider $r < -0.2$ or $r > 0.2$ as a moderate correlation

We then evaluated the association between different key measurements that were shown to be significant in other figures. Figure 4b illustrates the heatmap based on the Pearson correlation coefficient (−1 indicates a negative correlation, 1 indicates a positive correlation, and 0 indicates no correlation). We considered samples from different days collectively (e.g., the concave heatmap computed the samples together from Days 1, 2, 3, and 5) since the relationship between the measurements was assumed to be unchanged, which is manifested in our data in the above figures. We found that most measurement pairs showed a moderate correlation (e.g., the level of nuclear displacement is moderately correlated to both the level of total neurite length and YAP translocation) except for YAP intensity. Nonetheless, considering that each of the other measurements (i.e., total neurite length, nuclear displacement, YAP translocation) showed significant difference compared to the flat groups, this reinforced the idea that curvature is a mechanical stimulus that induces nuclear displacement, changes in YAP translocation, and neurite extension in the same cell, and the cause remains to be investigated.

Although we have shown that there was overall minimum change in the z-level of cells on curvature-substrates, the cell population at a specific range of z-levels may still manifest phenotypic changes that constitute the significant changes above (in other words, although cells were distributed evenly along the z-axis even on curvature-substrates, the cell behaviors may still be different along the z-axis). We therefore evaluated whether there were associations between various key measurements and its z-level in Fig. S3 (Supplementary Information). We found no consistent significant difference in the neurite extension direction (Fig. S3a in Supplementary Information; a significant difference would indicate that neurite outgrowth is restricted by curvature otherwise), nor was there a correlation between key phenotypes (total neurite length, YAP translocation, and nuclear displacement) and their corresponding z-position (Fig. S3b in Supplementary Information). This further reinforced the idea that our curvature samples did not interact with the cell bodies but rather with subcellular changes (as also noted in Sect. "Changes in whole-cell morphology of neural cells on curvature-substrates").

Changes in neural cell differentiation on curvature-substrates

Since we identified collective phenotypic changes in mechanotransduction and neural differentiation, we then proceeded to evaluate using more specific neural markers by staining the cells with Tuj-1 and GFAP (instead of F-actin and YAP). Both of them are intermediate neural markers, where GFAP is a neurofilament protein that is expressed transiently during neuronal differentiation and persistently during astrocytic differentiation [52], and Class-III β-tubulin (stained by Tuj-1) is a neurotubule protein that constitutes the cytoskeleton of neurites [53, 54]. Both of them have also been shown to be upregulated in N2a cells during induced differentiation [55, 56, 57].

The Tuj-1 neural marker was used to quantify neurites more clearly and functionally than F-actin (although F-actin drives and colocalizes with microtubule polymerization, it manifests as an actin wave that distributes less evenly along the neurite compared to microtubule proteins [58,59,60]). Figure 5 shows the results. Similar to Fig. 2, we see a lower cell density and clearer neurite growth in the curvature-substrates than in the flat substrates. Since Tuj-1 constitutes a major component of differentiating neural cells, we further evaluated their area and volume (Figs. S4a and S4b in Supplementary Information), and it manifested a similar result as their actin counterparts (Fig. S2 in Supplementary Information, mean cell volume in curvature-substrates is significantly higher than in the flat substrates). We then characterized the expression level of morphological differentiation in curvature-substrates, and indeed, we found a consistently higher Tuj-1 integrated intensity in curvature-substrates than in flat substrates (with concave and convex substrates again having smaller and inconsistent differences) (Fig. 5b). GFAP was also significantly higher in the curvature-substrates than in the flat substrate (Fig. 5c). Additionally, although the Tuj-1 intensity seems to be brighter in flat samples on Day 1 and Day 2 (Fig. 5a), this is simply due to the samples having an even lower GFAP intensity, which we further validated by computing the ratio of Tuj-1 intensity to GFAP intensity in Fig. S4c (Supplementary Information); the flat substrates indeed have a higher Tuj-1-GFAP ratio across different groups. This also confirmed that the Tuj-1 and GFAP intensities were associated, where cells in the curvature groups manifested both increased microtubule (according to Tuj-1) and GFAP expression. Overall, our results indicated better and more complete morphological differentiation in the curvature-substrates than in the flat substrates.

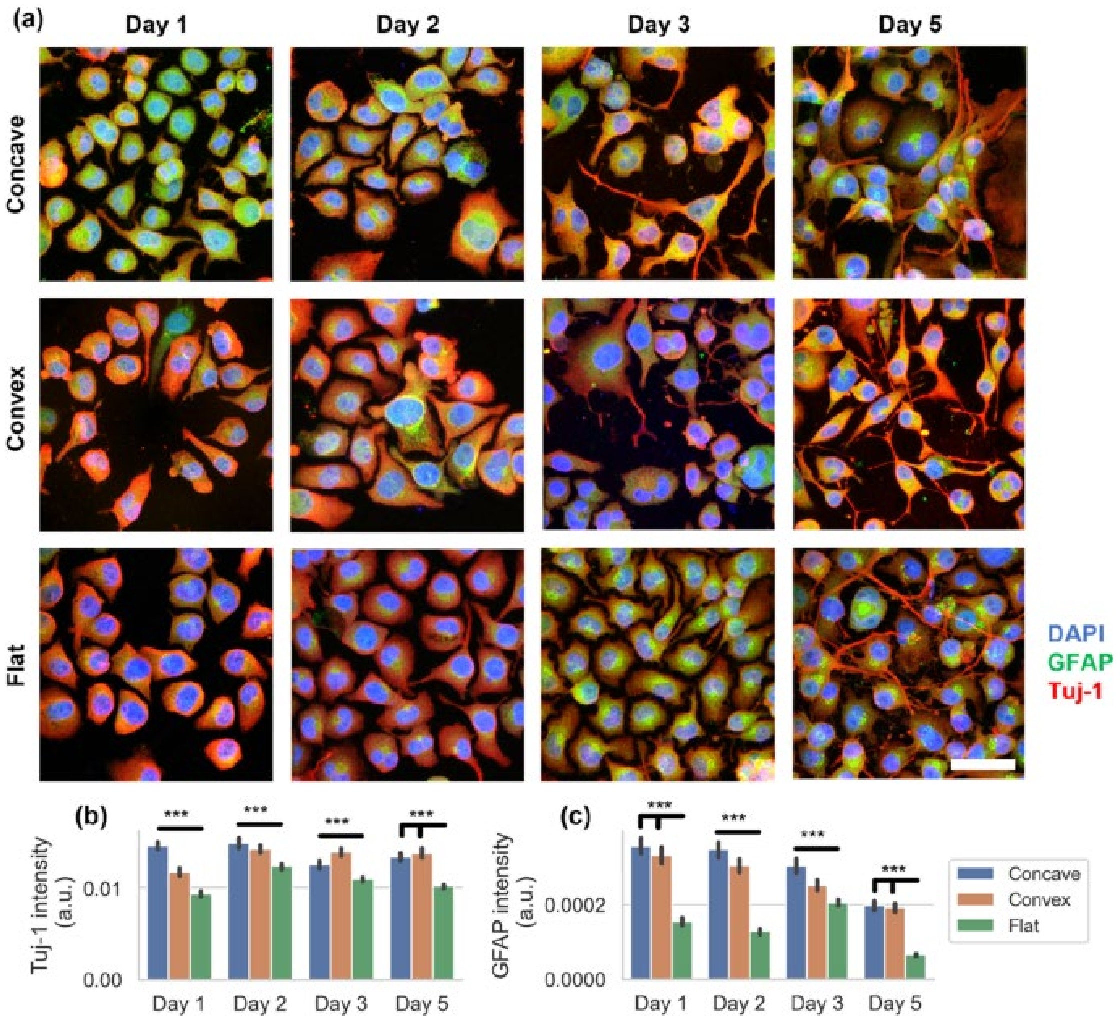

Fig. 5

Representative samples and measurements related to the neural differentiation markers of each group. **a** Representative *z*-projected fluorescent samples with nuclear (blue), GFAP (green), and Tuj-1 (red) staining. Scale bar: 50 μm. The mean integrated intensities of **b** Tuj-1-stained and **c** GFAP-stained areas among the cells in each group. Normalization details are discussed in Sect. "Quantitative methods for immunocytochemistry". A horizontal statistical bar indicates statistical significance among all pairs of samples (otherwise only the indicated pairs), $***p<0.001$. The error bar indicates ci=99%

Since the Tuj-1 marker characterizes neurite details more clearly, we further expanded our previous investigation on neurite features, as shown in Fig. 6. We found that the difference between the total neurite length in the curvature groups compared to the flat groups was significantly higher than the data using the F-actin-stained area (Figs. 6a and 6b). We also characterized neurite complexity (i.e., the level of neurite branching, Fig. 6c), and similarly, we found that the neurites in the curvature groups were significantly more complex. Both further support the enhanced differentiation in curvature groups. Examining the cells with the highest total neurite length, we indeed observed more complex and longer neurites for cells in the curvature groups, and in particular, there were more cells with zero total neurite length in the flat groups than in the curvature groups (Table S2 in Supplementary Information).

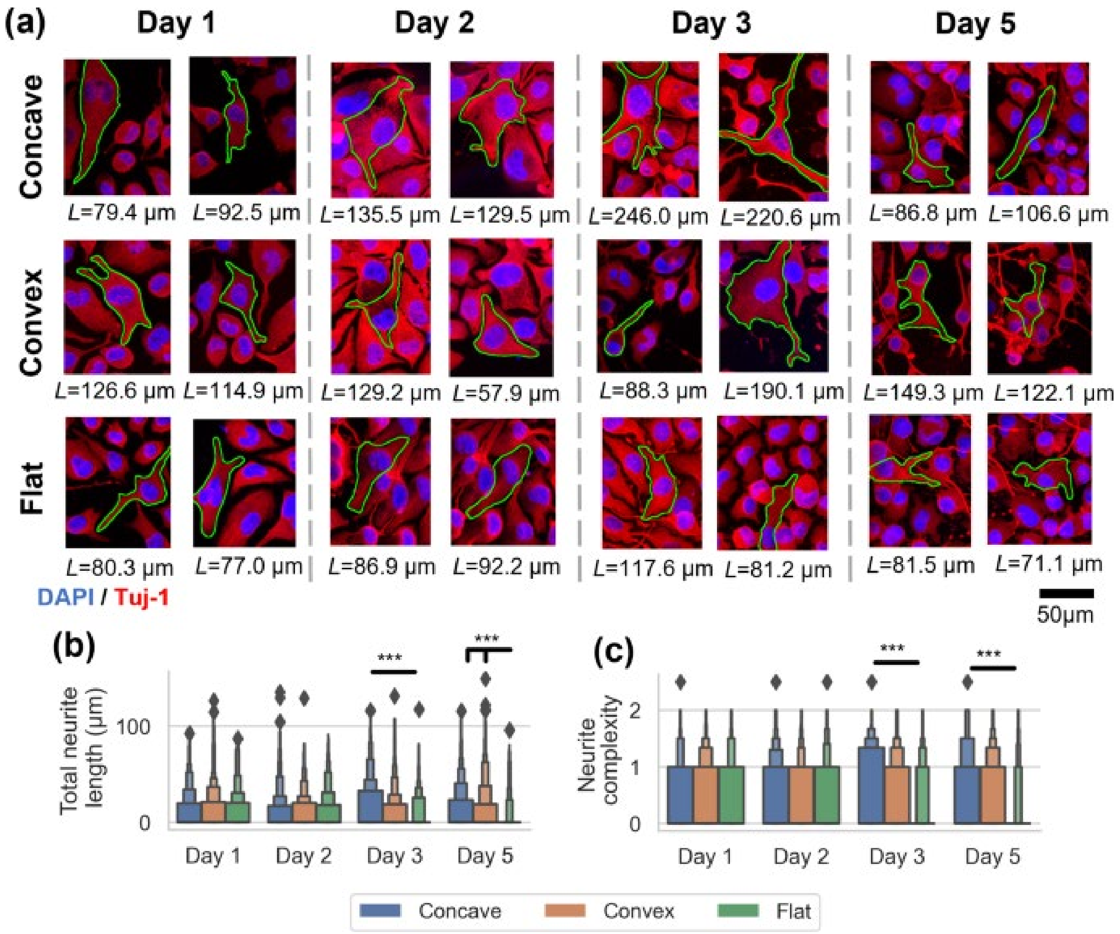

Fig. 6

Neurite outgrowth in neural cells on curvature-substrates. **a** *z*-projected representative samples. In each group, 10 samples with the highest total neurite length were examined, and two representative samples were selected for the figures. The outer green outline depicts the identified cells, determined algorithmically. See Sect. "Quantitative methods for immunocytochemistry" for details; *L* shows the total neurite length. Boxen plots illustrate the population distribution of **b** mean total neurite length and **c** neurite complexity for cells of each group. A single data point depicts the outliers. Statistical details are arranged the same way as the other figures. A horizontal statistical bar indicates statistical significance among all pairs of samples (otherwise only the indicated pairs), ***$p<0.001$. The error bar indicates ci=99%

Discussion

In this study, we showed that microcurvature induced better morphological differentiation, as demonstrated in several aspects, including increased nuclear displacement, increased total neurite length, and increased YAP, Tuj-1, and GFAP expression (summarized in Table 1). We have also shown that both concave and convex substrates possessed similar curvature effects. This curvature effect was also unlike many of the other recent studies, where our samples showed minimum morphological changes to the main cell bodies. Thus, nuclear deformation and F-actin tension were excluded as the main mechanisms of the curvature effect. There were two possible reasons in combination for the absence of these effects. First, curvature as a mechanical stimulus highly depends on the material mechanics to begin with [8], and our results imply that our curvature-substrates have a low surface contractility and/or a high surface adhesion strength to the cells due to both the surface coating (laminin coating specifically) and the curvature parameter. Second, and perhaps most importantly, the cell type limited how curvature affects its behaviors. Most recent studies have focused on the curvature effect on osteogenesis in the form of mesenchymal stem cells [19, 61, 62], with some also using a similar curvature κ� at a similar scale as in our study (e.g., 1/82.5 μm^{-1} [18], 1/125 μm^{-1} [16]). However, for neural cells, the factor that is known to be most decisive is to establish neuronal polarity by guiding neurite outgrowth [63]. This is usually achieved by microgrooves [64], but the curvature of microrods [14, 15] or microchannels [10, 13] has also been shown to inhibit neurite outgrowth to some extent (which also depends on the type of neuronal cells [15]). Although there have been studies on the effect of the 3D curvature landscape on neural differentiation [20], the molecular mechanisms were not investigated. Therefore, our study provided comprehensive physical descriptions for neural cells on curvature-substrates using a similar curvature κ� as in other studies, and we established that 3D curvature landscapes enhanced neural differentiation, unlike other studies that focused on the 2D aspect (the neurite-limiting aspect) of curvature. Finally, although we did not elucidate the upstream mechanism in this study, among the key properties that were significantly regulated due to curvature, we believe that increased nuclear displacement is the most essential event that improves neuronal polarity, which is supported by many studies centralizing the role of the centrosome in neuronal differentiation (the centrosome regulates nuclear localization mechanically to establish asymmetry and hence neurite outgrowth) [65, 66, 67]. The molecular details remain to be elucidated in further studies. Altogether, this study documented enhanced neural differentiation using 3D curvature landscapes for possible tissue engineering applications in the future.

Table 1 Summary depicting key measurements with significant changes to neural cells seeded onto the curvature-substrates compared to flat substrates

	Physical changes	Other phenotypic changes
Curvature-substrates	• Inscreased total neurite length	• Increased YAP intensity
	• Increased nuclear displacement	• Decreased YAP translocation

	• Increased neurite complexity	• Increased Tuj-1 intensity
		• Increased GFAP intensity

References

1. Dunn GA, Heath JP (1976) A new hypothesis of contact guidance in tissue cells. Exp Cell Res 101(1):1–14. https://doi.org/10.1016/0014-4827(76)90405-5
2. Curtis ASG, Varde M (1964) Control of cell behavior: topological factors. J Natl Cancer Inst 33(1):15–26. https://doi.org/10.1093/jnci/33.1.15
3. Baptista D, Teixeira L, van Blitterswijk C et al (2019) Overlooked? Underestimated? Effects of substrate curvature on cell behavior. Trends Biotechnol 37(8):838–854. https://doi.org/10.1016/j.tibtech.2019.01.006
4. Pelham RJ Jr, Wang YL (1997) Cell locomotion and focal adhesions are regulated by substrate flexibility. Proc Natl Acad Sci USA 94(25):13661–13665. https://doi.org/10.1073/pnas.94.25.13661
5. Ye K, Wang X, Cao L et al (2015) Matrix stiffness and nanoscale spatial organization of cell-adhesive ligands direct stem cell fate. Nano Lett 15(7):4720–4729. https://doi.org/10.1021/acs.nanolett.5b01619
6. Cavalcanti-Adam EA, Volberg T, Micoulet A et al (2007) Cell spreading and focal adhesion dynamics are regulated by spacing of integrin ligands. Biophys J 92(8):2964–2974. https://doi.org/10.1529/biophysj.106.089730
7. Boyan BD, Hummert TW, Dean DD et al (1996) Role of material surfaces in regulating bone and cartilage cell response. Biomaterials 17(2):137–146. https://doi.org/10.1016/0142-9612(96)85758-9
8. Yamashita T, Kollmannsberger P, Mawatari K et al (2016) Cell sheet mechanics: how geometrical constraints induce the detachment of cell sheets from concave surfaces. Acta Biomater 45:85–97. https://doi.org/10.1016/j.actbio.2016.08.044
9. Alias MA, Buenzli PR (2017) Modeling the effect of curvature on the collective behavior of cells growing new tissue. Biophys J 112(1):193–204. https://doi.org/10.1016/j.bpj.2016.11.3203
10. Khan H, Beck C, Kunze A (2021) Multi-curvature micropatterns unveil

distinct calcium and mitochondrial dynamics in neuronal networks. Lab Chip 21(6):1164 - 1174. https://doi.org/10.1039/d0lc01205j

11. Hilgetag CC, Barbas H (2006) Role of mechanical factors in the morphology of the primate cerebral cortex. PLoS Comput Biol 2(3):e22. https://doi.org/10.1371/journal.pcbi.0020022
12. Del Toro D, Ruff T, Cederfjäll E et al (2017) Regulation of cerebral cortex folding by controlling neuronal migration via FLRT adhesion molecules. Cell 169(4):621-635.e16. https://doi.org/10.1016/j.cell.2017.04.012
13. Roth S, Bisbal M, Brocard J et al (2012) How morphological constraints affect axonal polarity in mouse neurons. PLoS ONE 7(3):e33623. https://doi.org/10.1371/journal.pone.0033623
14. Smeal RM, Rabbitt R, Biran R et al (2005) Substrate curvature influences the direction of nerve outgrowth. Ann Biomed Eng 33(3):376 - 382. https://doi.org/10.1007/s10439-005-1740-z
15. Smeal RM, Tresco PA (2008) The influence of substrate curvature on neurite outgrowth is cell type dependent. Exp Neurol 213(2):281 - 292. https://doi.org/10.1016/j.expneurol.2008.05.026
16. Werner M, Blanquer SB, Haimi SP et al (2016) Surface curvature differentially regulates stem cell migration and differentiation via altered attachment morphology and nuclear deformation. Adv Sci 4(2):1600347. https://doi.org/10.1002/advs.201600347
17. Pieuchot L, Marteau J, Guignandon A et al (2018) Curvotaxis directs cell migration through cell-scale curvature landscapes. Nat Commun 9(1):3995. https://doi.org/10.1038/s41467-018-06494-6
18. Jin ZY, Zhai YS, Zhou Y et al (2022) Regulation of mesenchymal stem cell osteogenic potential via microfluidic manipulation of microcarrier surface curvature. Chem Eng J 448:137739. https://doi.org/10.1016/j.cej.2022.137739
19. Yang Y, Xu T, Bei HP et al (2022) Gaussian curvature-driven direction of cell fate toward osteogenesis with triply periodic minimal surface scaffolds. Proc Natl Acad Sci USA 119(41):e2206684119. https://doi.org/10.1073/pnas.2206684119
20. Moe AA, Suryana M, Marcy G et al (2012) Microarray with micro- and nano-topographies enables identification of the optimal topography for directing the differentiation of primary murine neural progenitor cells. Small 8(19):3050 - 3061. https://doi.org/10.1002/smll.201200490
21. Conover JC, Notti RQ (2008) The neural stem cell niche. Cell Tissue Res 331(1):211 - 224. https://doi.org/10.1007/s00441-007-0503-6
22. Gu X, Ding F, Williams DF (2014) Neural tissue engineering options for peripheral nerve regeneration. Biomaterials 35(24):6143 - 6156. https://doi.org/10.1016/j.biomaterials.2014.04.064
23. Boni R, Ali A, Shavandi A et al (2018) Current and novel polymeric biomaterials for neural tissue engineering. J Biomed Sci

25(1):90. https://doi.org/10.1186/s12929-018-0491-8

24. Khademhosseini A, Langer R, Borenstein J et al (2006) Microscale technologies for tissue engineering and biology. Proc Natl Acad Sci USA 103(8):2480 - 2487. https://doi.org/10.1073/pnas.0507681102
25. Virtanen P, Gommers R, Oliphant TE et al (2020) SciPy 1.0: fundamental algorithms for scientific computing in Python. Nat Methods 17(3):261 - 272. https://doi.org/10.1038/s41592-019-0686-2
26. Wu G, Fang Y, Lu ZH et al (1998) Induction of axon-like and dendrite-like processes in neuroblastoma cells. J Neurocytol 27(1):1 - 14. https://doi.org/10.1023/a:1006910001869
27. Shea TB, Fischer I, Sapirstein VS (1985) Effect of retinoic acid on growth and morphological differentiation of mouse NB2a neuroblastoma cells in culture. Brain Res 353(2):307 - 314. https://doi.org/10.1016/0165-3806(85)90220-2
28. Stringer C, Wang T, Michaelos M et al (2021) Cellpose: a generalist algorithm for cellular segmentation. Nat Methods 18(1):100 - 106. https://doi.org/10.1038/s41592-020-01018-x
29. Ho SY, Chao CY, Huang HL et al (2011) NeurphologyJ: an automatic neuronal morphology quantification method and its application in pharmacological discovery. BMC Bioinform 12:230. https://doi.org/10.1186/1471-2105-12-230
30. Zhang TY, Suen CY (1984) A fast parallel algorithm for thinning digital patterns. Commun ACM 27(3):236 - 239. https://doi.org/10.1145/357994.358023
31. Sun J, Wang D, Guo L et al (2017) Androgen receptor regulates the growth of neuroblastoma cells in vitro and in vivo. Front Neurosci 11:116. https://doi.org/10.3389/fnins.2017.00116
32. Tremblay RG, Sikorska M, Sandhu JK et al (2010) Differentiation of mouse Neuro 2A cells into dopamine neurons. J Neurosci Methods 186(1):60 - 67. https://doi.org/10.1016/j.jneumeth.2009.11.004
33. Marzinke MA, Clagett-Dame M (2012) The all-trans retinoic acid (atRA)-regulated gene Calmin (*Clmn*) regulates cell cycle exit and neurite outgrowth in murine neuroblastoma (Neuro2a) cells. Exp Cell Res 318(1):85 - 93. https://doi.org/10.1016/j.yexcr.2011.10.002
34. Su X, Gu X, Zhang Z et al (2020) Retinoic acid receptor gamma is targeted by microRNA-124 and inhibits neurite outgrowth. Neuropharmacology 163:107657. https://doi.org/10.1016/j.neuropharm.2019.05.034
35. Vining KH, Mooney DJ (2017) Mechanical forces direct stem cell behaviour in development and regeneration. Nat Rev Mol Cell Biol 18(12):728 - 742. https://doi.org/10.1038/nrm.2017.108
36. Tojkander S, Gateva G, Lappalainen P (2012) Actin stress fibers—assembly, dynamics and biological roles. J Cell Sci 125(Pt 8):1855 - 1864. https://doi.org/10.1242/jcs.098087
37. Olson EN, Nordheim A (2010) Linking actin dynamics and gene transcription

to drive cellular motile functions. Nat Rev Mol Cell Biol 11(5):353–365. https://doi.org/10.1038/nrm2890

38. Kalukula Y, Stephens AD, Lammerding J et al (2022) Mechanics and functional consequences of nuclear deformations. Nat Rev Mol Cell Biol 23(9):583–602. https://doi.org/10.1038/s41580-022-00480-z
39. Panciera T, Azzolin L, Cordenonsi M et al (2017) Mechanobiology of YAP and TAZ in physiology and disease. Nat Rev Mol Cell Biol 18(12):758–770. https://doi.org/10.1038/nrm.2017.87
40. Dupont S, Morsut L, Aragona M et al (2011) Role of YAP/TAZ in mechanotransduction. Nature 474(7350):179–183. https://doi.org/10.1038/nature10137
41. Zhang H, Deo M, Thompson RC et al (2012) Negative regulation of Yap during neuronal differentiation. Dev Biol 361(1):103–115. https://doi.org/10.1016/j.ydbio.2011.10.017
42. Sun Y, Yong KM, Villa-Diaz LG et al (2014) Hippo/YAP-mediated rigidity-dependent motor neuron differentiation of human pluripotent stem cells. Nat Mater 13(6):599–604. https://doi.org/10.1038/nmat3945
43. Lin YT, Ding JY, Li MY et al (2012) YAP regulates neuronal differentiation through Sonic hedgehog signaling pathway. Exp Cell Res 318(15):1877–1888. https://doi.org/10.1016/j.yexcr.2012.05.005
44. Yamada KM, Sixt M (2019) Mechanisms of 3D cell migration. Nat Rev Mol Cell Biol 20(12):738–752. https://doi.org/10.1038/s41580-019-0172-9
45. Gundersen GG, Worman HJ (2013) Nuclear positioning. Cell 152(6):1376–1389. https://doi.org/10.1016/j.cell.2013.02.031
46. Davidson PM, Cadot B (2021) Actin on and around the Nucleus. Trends Cell Biol 31(3):211–223. https://doi.org/10.1016/j.tcb.2020.11.009
47. Cáceres A, Ye B, Dotti CG (2012) Neuronal polarity: demarcation, growth and commitment. Curr Opin Cell Biol 24(4):547–553. https://doi.org/10.1016/j.ceb.2012.05.011
48. Meiring JCM, Shneyer BI, Akhmanova A (2020) Generation and regulation of microtubule network asymmetry to drive cell polarity. Curr Opin Cell Biol 62:86–95. https://doi.org/10.1016/j.ceb.2019.10.004
49. Lee Y, McIntire LV, Zygourakis K (1994) Analysis of endothelial cell locomotion: differential effects of motility and contact inhibition. Biotechnol Bioeng 43(7):622–634. https://doi.org/10.1002/bit.260430712
50. Su J, Zapata PJ, Chen CC et al (2009) Local cell metrics: a novel method for analysis of cell-cell interactions. BMC Bioinform 10:350. https://doi.org/10.1186/1471-2105-10-350
51. Moore R, Theveneau E, Pozzi S et al (2013) Par3 controls neural crest migration by promoting microtubule catastrophe during contact inhibition of locomotion. Development 140(23):4763–4775. https://doi.org/10.1242/dev.098509
52. Dimou L, Götz M (2014) Glial cells as progenitors and stem cells: new roles in the healthy and diseased brain. Physiol Rev 94(3):709–

737. https://doi.org/10.1152/physrev.00036.2013

53. Chan KY, Baxter CF (1979) Compartments of tubulin and tubulin-like proteins in differentiating neubroblastoma cells. Brain Res 174(1):135-152. https://doi.org/10.1016/0006-8993(79)90809-6

54. Katsetos CD, Karkavelas G, Herman MM et al (1998) Class III beta-tubulin isotype (beta III) in the adrenal medulla: I. localization in the developing human adrenal medulla. Anat Rec 250(3):335-343

55. Wu PY, Lin YC, Chang CL et al (2009) Functional decreases in P2X7 receptors are associated with retinoic acid-induced neuronal differentiation of Neuro-2a neuroblastoma cells. Cell Signal 21(6):881-891. https://doi.org/10.1016/j.cellsig.2009.01.036

56. Jeon WB, Park BH, Choi SK et al (2012) Functional enhancement of neuronal cell behaviors and differentiation by elastin-mimetic recombinant protein presenting Arg-Gly-Asp peptides. BMC Biotechnol 12:61. https://doi.org/10.1186/1472-6750-12-61

57. Choi SK, Kim JH, Park JK et al (2013) Cytotoxicity and inhibition of intercellular interaction in N2a neurospheroids by perfluorooctanoic acid and perfluorooctanesulfonic acid. Food Chem Toxicol 60:520-529. https://doi.org/10.1016/j.fct.2013.07.070

58. Dehmelt L, Halpain S (2004) Actin and microtubules in neurite initiation: are MAPs the missing link? J Neurobiol 58(1):18-33. https://doi.org/10.1002/neu.10284

59. Winans AM, Collins SR, Meyer T (2016) Waves of actin and microtubule polymerization drive microtubule-based transport and neurite growth before single axon formation. eLife 5:e12387. https://doi.org/10.7554/eLife.12387

60. Konietzny A, Bär J, Mikhaylova M (2017) Dendritic actin cytoskeleton: structure, functions, and regulations. Front Cell Neurosci 11:147. https://doi.org/10.3389/fncel.2017.00147

61. Liu W, Sun Q, Zheng ZL et al (2022) Topographic cues guiding cell polarization via distinct cellular mechanosensing pathways. Small 18(2):e2104328. https://doi.org/10.1002/smll.202104328

62. Liu Y, Yang Q, Wang Y et al (2022) Metallic scaffold with micron-scale geometrical cues promotes osteogenesis and angiogenesis via the ROCK/Myosin/YAP pathway. ACS Biomater Sci Eng 8(8):3498-3514. https://doi.org/10.1021/acsbiomaterials.2c00225

63. Yogev S, Shen K (2017) Establishing neuronal polarity with environmental and intrinsic mechanisms. Neuron 96(3):638-650. https://doi.org/10.1016/j.neuron.2017.10.021

64. Ferrari A, Cecchini M, Dhawan A et al (2011) Nanotopographic control of neuronal polarity. Nano Lett 11(2):505-511. https://doi.org/10.1021/nl103349s

65. Higginbotham HR, Gleeson JG (2007) The centrosome in neuronal development. Trends Neurosci 30(6):276-

283. https://doi.org/10.1016/j.tins.2007.04.001

66. Elric J, Etienne-Manneville S (2014) Centrosome positioning in polarized cells: common themes and variations. Exp Cell Res 328(2):240–248. https://doi.org/10.1016/j.yexcr.2014.09.004

67. Holcomb PS, Deerinck TJ, Ellisman MH et al (2013) Construction of a polarized neuron. J Physiol 591(13):3145–3150. https://doi.org/10.1113/jphysiol.2012.248542